ACS OMEGA

http://pubs.acs.org/journal/acsodf

Article

Porous Cobalt Sulfide Selenium Nanorods for Electrochemical Hydrogen Evolution

Zhengtian Shi,[†] Xiangqian Qi,[†] Zhiyuan Zhang,[†] Yingchao Song, Jianfa Zhang, Chucai Guo, and Zhihong Zhu*

Cite This: *ACS Omega* 2021, 6, 23300−23310

Read Online

ACCESS | Metrics & More | Article Recommendations | Supporting Information

ABSTRACT: A key process in electrochemical energy technology is hydrogen evolution reaction (HER). However, its electrochemical properties mainly depend on the catalytic activity of the material itself. Therefore, it is important to find efficient electrocatalysts to realize clean hydrogen production. As a typical kind of catalytic materials, transition metal dichalcogenides (TMCs) play important roles in the field of energy catalysis. As a representative of TMCs, cobalt disulfide (CoS_2), recently has raised much research interest owing to its abundant reserves, environmental friendliness, and excellent electrochemical stability. Meanwhile, given the fact that doping is one of the effective methods to improve the electrochemical catalytic property, various means of doping have been researched. Here, we report for the first time that porous-like Se−CoS_{2-x} (or Se:CoS_{2-x}) nanorod can be facilely synthesized via a controllable two-step strategy. It is demonstrated that doping Se can greatly improve the catalytic performance of CoS_2 electrode. The electrode can obtain a current density of 10 mA cm^{-2} at overpotential of only ∼260 mV. And the current changes with the applied bias voltage in an obvious stepped pattern, in the chronopotential (CP) curve of Se−CoS_{2-x}, indicating its outstanding mass transfer property and mechanical stability.

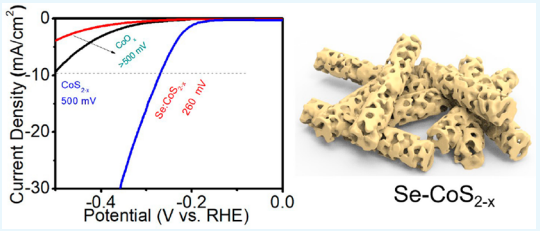

INTRODUCTION

When it comes to the current energy problem, conventional energies such as coal, petroleum, natural gas fail to provide a feasible solution for their shortcomings of being nonrenewable, pollutional, and harmful during the combustion process.[1−3] That is why it is necessary to seek new renewable clean energy sources, among which, hydrogen may act as a perfect candidate. The most direct approach to obtain hydrogen is splitting water.[4] However, a certain amount of energy (such as additional bias voltage) is required during this process. Therefore, to realize clean hydrogen production, high-efficiency catalysts have been researched in recent years, e.g., platinum- (Pt-) based alloys.[5−7] Nevertheless, although high-performance, the expensive cost and limited reserves of Pt metals have restricted its application for industrial hydrogen production. Thus, synthesis of a catalyst composed of earth-abundance, eco-friendly, and inexpensive elements is essential. Over the past 2 decades, TMCs MX_2 (M = Mo, W, Co, Ni, etc.; X = S, Se, etc.) have been widely used in electrochemical devices. For example, MoS_2,[8−10] $MoSe_2$,[11,12] WS_2,[13,14] CoS_2,[15−19] and other catalysts,[20−23] among which is cobalt pyrite (CoS_2, $CoSe_2$), a typical pyrite-type transition metal dichalcogenide,[24−30] have already been widely used in the field of electrochemistry due to their unique advantages. Meanwhile, the properties of electrochemical devices are closely related to the structure of materials. Therefore, in recent years, scientists have been trying to develop new techniques for synthesizing different structures such as nanoparticles,[31] nanosheets,[32−34] nanocrystals,[35] nanoboxes,[36,37] nanowires,[38] and so on. Nonetheless, the performance of pure CoS_2 is still insufficient due to lack of active sites and low conductivity. For this reason, it is quite important to adopt a novel strategy to develop electrochemical devices with high-efficiency, super-stability, and superior electrochemical performance.

Previous studies have shown that moderate doping can effectively improve the electrochemical catalytic activities, e.g., N,[39−45] P,[46−50] Ni,[51] Fe,[52,53] Al,[54] Se,[55] Mn,[56] and so on. Therein, the performances of selenide products are much better than those of other products (e.g., sulfur), which may be ascribed to the following reasons: (i) the Se atom has larger electronegativity than the S atom, and the Se atom can substitute the S atom during a high temperature reaction process; (ii) Se (compared to S) forms a new bond with another element, which causes the lattice spacing to change, facilitating electron conduction at the solution interface, and finally improves the catalytic performance. Therefore, selenium doping is one of the most important means to improve

Received: June 9, 2021
Accepted: July 23, 2021
Published: September 2, 2021

Scheme 1. Schematic Diagram of Preparation Procedures of Different Samples

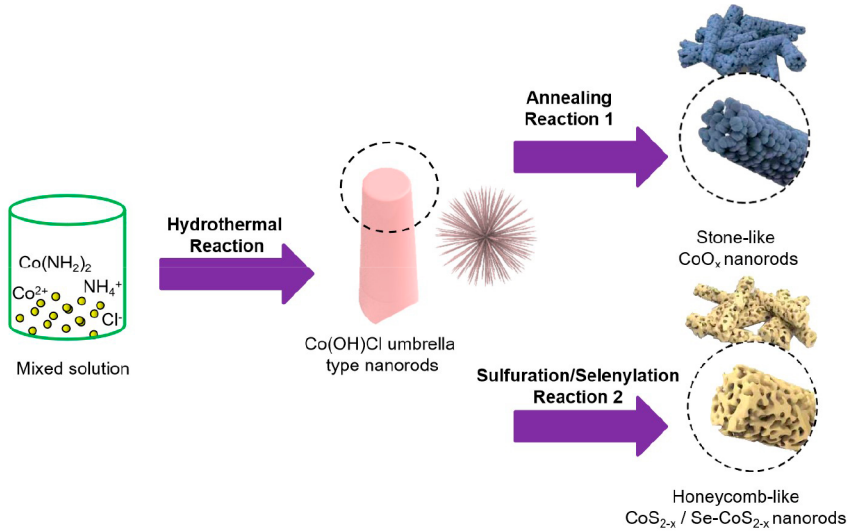

performances of electrochemical catalytic devices. However, as far as we know, the Se dopants are rarely reported, possibly attributed to their uncontrollable preparation process and relatively high cost.

In this work, the porous-like Se−CoS_{2-x} nanorod is successfully synthesized via a simple two-step method. The first step is to synthesize umbrella-type Co(OH)Cl nanorods (Co(OH)Cl UNs) as precursor by low temperature hydrothermal reaction. The second step is sulfuration/selenylation at 400 °C for 1h. Specific reaction processes are as follows:

$$Co^{2+} + Cl^{-} \rightarrow CoCl^{+} \quad (1)$$

$$CO(NH_2)_2 + 3H_2O \rightarrow 2NH_4^{+} + 2OH^{-} + CO_2 \quad (2)$$

$$CoCl^{+} + OH^{-} \rightarrow Co(OH)Cl \quad (3)$$

$$Co + (2 - x)S \rightarrow CoS_{2-x} \quad (4)$$

$$Co + (2 - x)S + ySe \rightarrow CoS_{2-x}Se_y \quad (5)$$

The result indicates that the Se−CoS_{2-x} catalyst effectively improves the speed of electron transfer, showing much better electrocatalytic performance than that of CoO_x and CoS_{2-x} catalysts.

RESULTS AND DISCUSSION

The fabrication of Se doped CoS_{2-x} electrodes is schematically depicted in Scheme 1. The electrodes are prepared via a sequential two-step approach: (i) Co(OH)Cl UNs are synthesized through a simple hydrothermal growth process; (ii_{-1}) CoO_x electrode is obtained by calcination of the Co(OH)Cl UNs precursor; (ii_{-2}) CoS_{2-x} electrode is obtained by low-temperature sulfuration of the Co(OH)Cl UNs precursor; (ii_{-3}) Se−CoS_{2-x} electrode is obtained by low-temperature hybrid sulfuration−selenylation of the Co(OH)Cl precursor.

The formation of the product (CoO_x) may derive from the excessive decomposition of the Co(OH)Cl precursor during the reaction process. Figure 1a−f and Figure S1 present the SEM images of the CoO_x nanorods with the annealing temperature 400 °C. As shown in parts a and b of Figure 1, CoO_x exhibits a stone-like nanorods structure, with diameter of about 200−500 nm and a length of about 2−10 μm. Figure 1c reveals the energy dispersive X-ray (EDX) spectrum of the annealing product, where the ratio of Co to O is about 1:1.28, confirming the existence of CoO_x (x = 1.28). Distribution of different elements in the CoO_x nanorods is analyzed through elemental mapping. Uniform distribution of Co, O, and C elements can be observed in the product, as illustrated in Figure 1d−f.

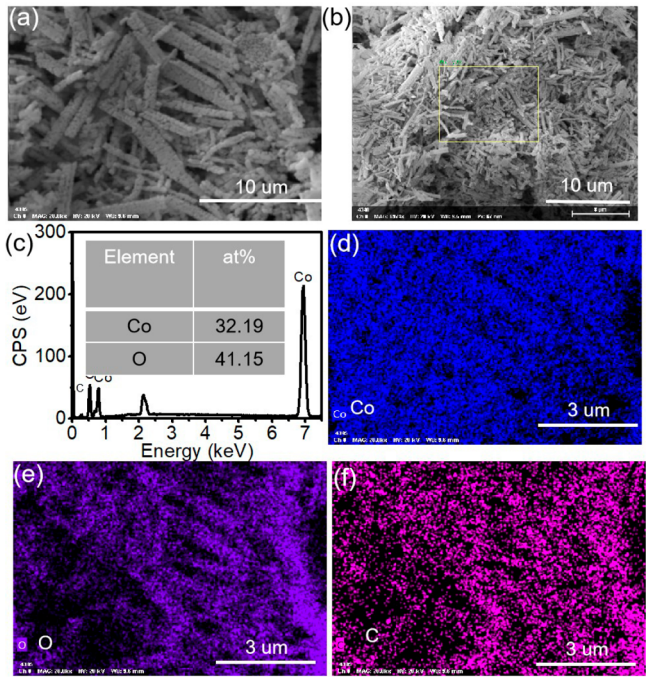

Figure 1. (a) SEM images of the CoO_x nanorods; (b) SEM images of the CoO_x nanorods in other regions; (c) EDX spectrum of the CoO_x nanorods, and elemental mapping of (d) Co, (e) O, and (f) C.

Parts a and b of Figure 2 are SEM images of the CoS_{2-x} electrode, showing 2−10 μm porous-rod-like structure stacked by nanoparticles, with some gaps exist between blocks and blocks. The EDX spectrum in Figure 2c reveals an atomic ratio of Co to S less than 1:2, namely CoS_{2-x}, confirming that some Co−S bonds in the product may break off or some sulfur

https://doi.org/10.1021/acsomega.1c03019
ACS Omega 2021, 6, 23300−23310

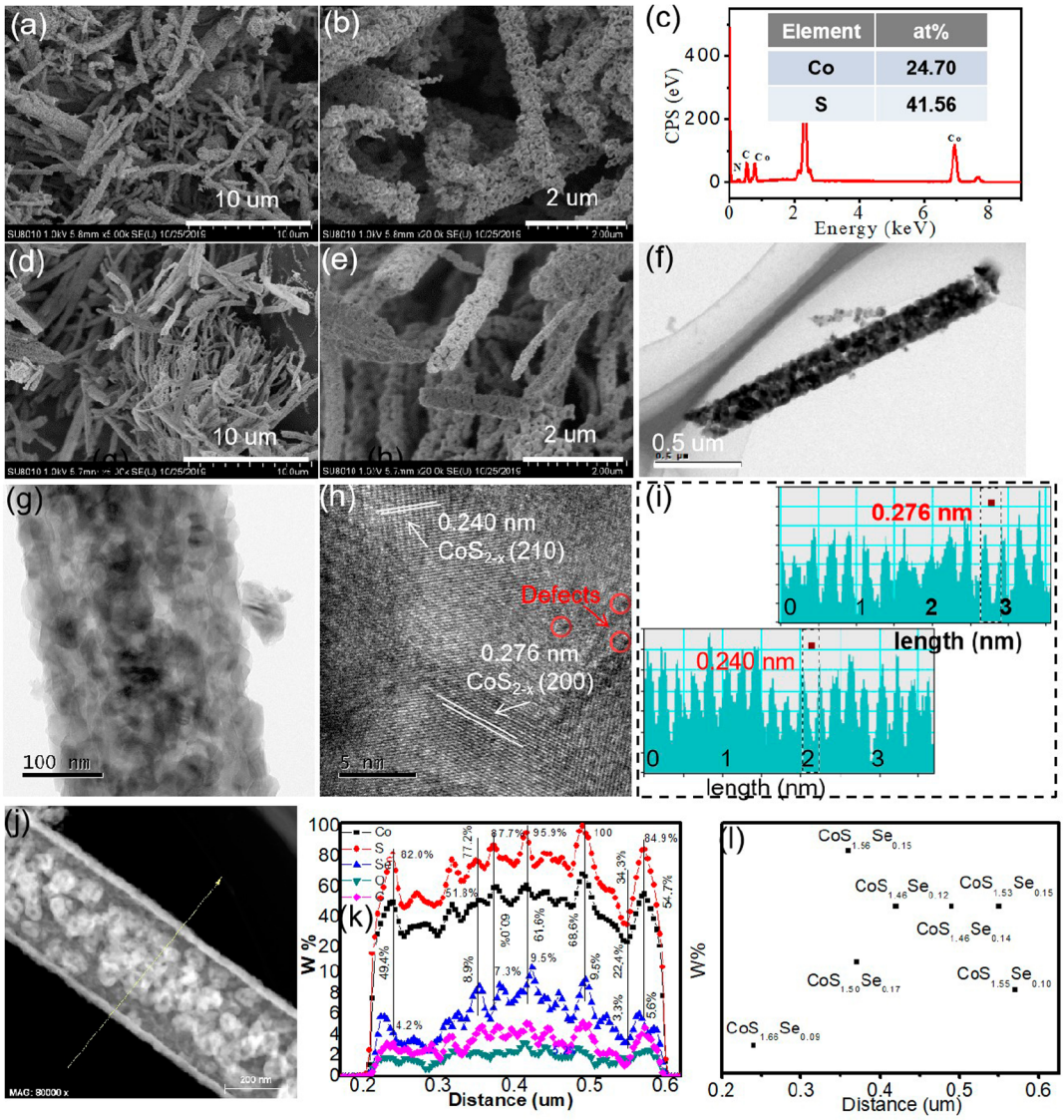

Figure 2. (a, b) SEM images, (c) EDX spectrum of the CoS_{2-x} sample; (d, e) FESEM, (f) TEM, (g, h) HRTEM images of the Se−CoS_{2-x} sample; (i) insert figure of HRTEM; (j–l) EDS line scan mapping of the Se−CoS_{2-x} sample.

vacancy is formed,[39] as later explained in Figure 3. Similar to the CoS_{2-x} electrode, SEM images of Se−CoS_{2-x} electrode as shown in parts d and e of Figure 2 also display a porous-rod-like structure, with diameter of about 200−500 nm and length of about 2−10 μm. As reference, the precursor Co(OH)Cl exhibits umbrella type nanorods structure, with a diameter of about 200−500 nm and a length of about 2−10 μm (Figure S2). For the microstructure of the Se−CoS_{2-x}, transmission electron microscopy (TEM) images are obtained as shown in Figure 2f–h. The TEM images in parts f and g of Figure 2 show that the Se−CoS_{2-x} catalyst is about 2 μm in length and about 200 nm in diameter. The high-resolution transmission electron microscopy (HRTEM) image (Figure 2h) reveals that the interplanar spacing of Se−CoS_{2-x} catalysts is 0.240 and 0.276 nm, corresponding to the (2 1 0) and (2 0 0) planes of CoS_{2-x}. In addition, no interfacial spacing of $CoSe_2$ is detected from HRTEM, indicating that Se has been successfully doped into CoS_{2-x}. Figure 2j–l and Figure S3 show EDS line scan mapping results of the Se−CoS_{2-x} nanorod. From the selected points, the atomic number ratio of Co and S fluctuates around 1:1.5, which may be caused by the sulfur vacancy or the interstitial doping of selenium in the process of sulfuration or selenization.

Formation of CoS_{2-x} and Se−CoS_{2-x} polyporous nanorods may be attributed to the defects, interstitial doping or atomic bond breaking during the sulfuration/selenization process (Figure 3). As shown in Figure 3a, the precursor Co(OH)Cl first forms CoS_2 during the sulfuration process at high temperature. Then sulfur vacancy or sulfur interstitially doping is generated as the reaction goes on, finally forming CoS_{2-x}. Similarly, as shown in Figure 3b, in the process of high temperature sulfuration/selenization, the precursor Co(OH)Cl is easy to form Se−CoS_{2-x} through random selenium doping (may be interstitial doping or in situ substitution). And sulfur vacancy or sulfur interstitially doping will be generated soon, leading to the formation of Se−CoS_{2-x}. According to the above analysis and Figure 3c, the formation mechanism can be explained based on the different reaction rates of Co^{2+}, OH^-, S, and Se: According to the molecular dynamics principle, the Co^{2+} peak makes it easy to form CoS_2 with S powder. After the formation of CoS_2, sulfur vacancy and sulfur bond fracture will occur during the reaction, thus forming CoS_{2-x}. In addition,

https://doi.org/10.1021/acsomega.1c03019
ACS Omega 2021, 6, 23300−23310

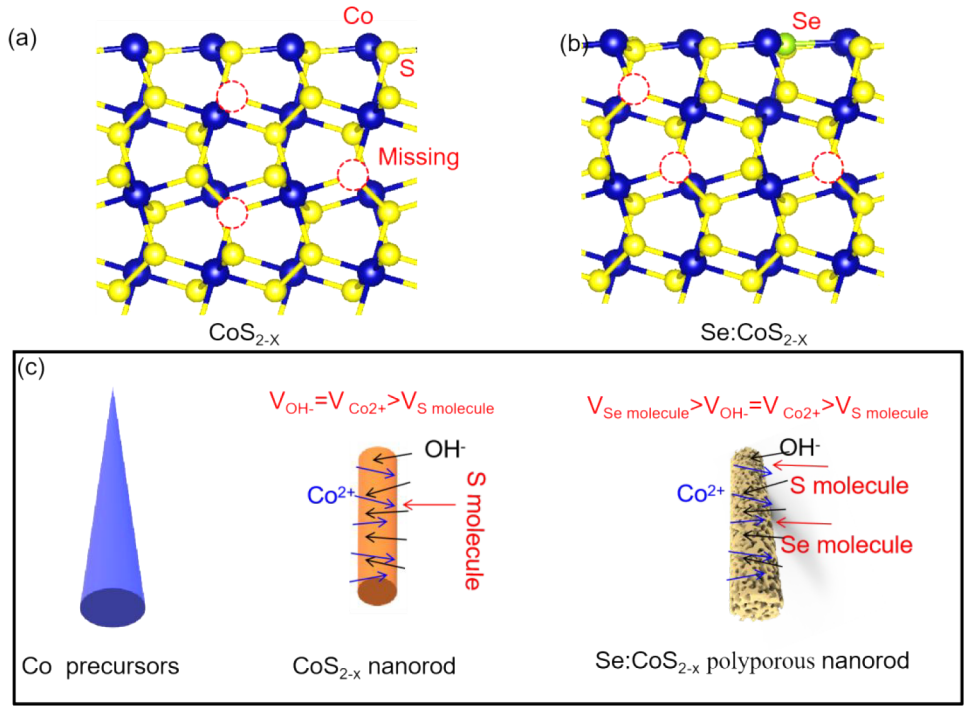

Figure 3. (a, b) Optimized atomic structures of CoS_{2-x} and Se−CoS_{2-x}, respectively. (c) Formation mechanism diagram of CoS_{2-x} nanorod and Se−CoS_{2-x} polyporous nanorod.

selenium also participates in the reaction. At high temperature, selenium atoms are very easy to replace sulfur atoms, or exist in the form of interstitial doping, thus forming Se−CoS_{2-x}. The increased numbers of active sites due to the effect of selenium doping make important contribution to subsequent electrochemical performance improvement.

The XRD patterns of CoS_{2-x} and Se−CoS_{2-x} catalysts are shown in Figure 4a, where the peaks at 27.2°, 32.3°, 36.3°, 55.1°, and 62.2° are indexed to (111), (200), (210), (311), and (321) planes of CoS_2 (JCPDS 41-1471),[16] respectively. Peak value of the obtained product CoS_{2-x} does not change significantly, indicating that the structure of the product is not damaged under this condition. In addition, slight shift of peaks can be observed after doping Se, with no Se-related new phases, indicating the successful doping of Se element into the structure of CoS_{2-x}. Parts b−f of Figure 4 display XPS survey spectra of Co, S, Se, and O elements, respectively. The Co 2p can be divided into five peaks as indicated in Figure 4b, where two obvious peaks at 778.7 and 793.9 eV, corresponding to Co $2p_{3/2}$ and Co $2p_{1/2}$, are consistent with the previous report.[42] In addition, The peaks at 778.5 and 793.8 eV may correspond to the CoO_x bonding of the surface oxide in air, consistent with previous report.[26] Se doping leads peak shift to higher binding energy for about 0.4 eV, implying the formation of new Co−Se bonds, and indicating that Se doping effectively modifies the electronic structure of Co. In Figure 4c, peaks located at 55.7 and 54.2 eV are attributed to Se $3d_{3/2}$ and Se $3d_{5/2}$, respectively, close to the previously reported values of Se doped CoS_2.[53] And the broad peak located at 59.7 eV corresponds to the surface oxidation of the Se edges.[26] High-resolution spectra of S 2p shown in Figure 4d can be decomposed into three peaks, locating at 162.8 and 163.9 eV, assigned to S $2p_{3/2}$ and S $2p_{1/2}$, respectively, and locating at 168.9 eV, assigned to S surface oxide contamination in Se−CoS_{2-x}. As shown in Figure 4f, elements Co, S, Se, and O exist in a wide spectrum of 50−800 eV, where the detected O element by XPS may mainly attribute to the absorbed oxygen or hydroxyl group or adsorbed water in the samples. (Figure 4e).[32] The XPS results confirm that Se doping significantly influence the chemical state of Co and S.

In order to discuss the function of Se dopants on the HER process, a series of electrochemical hydrogen evolution experiment are carried out in 0.5 M H_2SO_4 solution using a three-electrode system. Specific reaction processes are as follows.

HER in acidic electrolyte gives[52]

$$\text{Volmer process: } H_3O^+ + X + e^- \rightarrow X{-}H_{ads} + H_2O \quad (6)$$

$$\text{Heyrovsky process: } X{-}H_{ads} + H_3O^+ + e^- \rightarrow H_2 + X + H_2O \quad (7)$$

$$\text{Tafel process: } 2X{-}H_{ads} \rightarrow 2X + H_2 \quad (8)$$

(*X stands for the surface active site, H_{ads} stands for the adsorbed hydrogen).

The LSV curve is an important measurement index in electrochemical reaction. Results of LSV measurements, as shown in parts a and b of Figure 5, reveal that Se−CoS_{2-x} electrode performs the best catalytic activities among all catalysts. Its overpotential of only ∼260 mV (under the current density of 10 mA cm^{-2}) is far lower than that of the CoS_{2-x} electrode (500 mV) and CoO_x (>500 mV). In all samples, it is obvious that the overpotential value of CoO_x is the largest, indicating that the sulfuration or selenization product can provide more active sites. The corresponding Tafel slope is then calculated, as shown in parts c and d of Figure 5, via the Tafel formula $y = m + n \log k$ (where y stands for the overpotential, m stands for the Tafel slope, n stands for the intercept, and k stands for the current density). The calculated slope of Se−CoS_{2-x} electrode is 89.9 mV dec^{-1}, implying faster

https://doi.org/10.1021/acsomega.1c03019
ACS Omega 2021, 6, 23300−23310

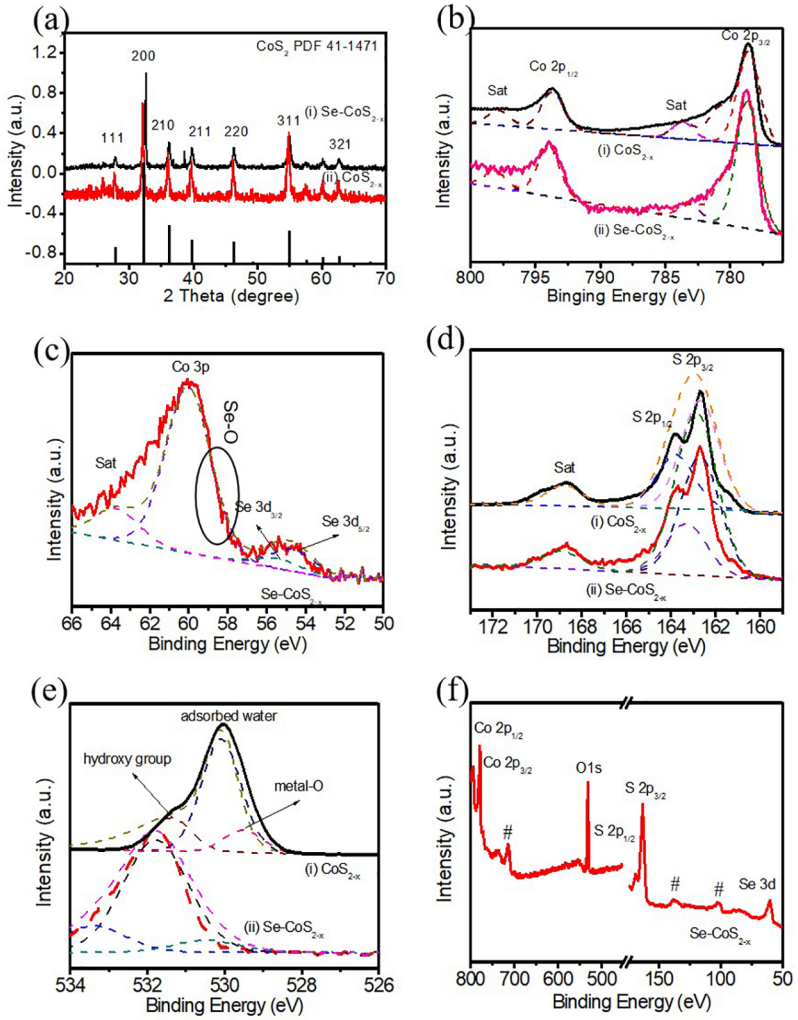

Figure 4. (a) XRD patterns of CoS_{2-x} and Se−CoS_{2-x} with standard peaks of CoS_2 listed. (b−f) XPS survey spectra of CoS_{2-x} and Se−CoS_{2-x}, Co 2p, Se 3d, S 2p, and O 1s, respectively.

proton transfer kinetics, which is conducive to the rapid progress of HER.

In addition, electrochemical impedance spectroscopy is applied for the CoO_x, CoS_{2-x}, Se−CoS_{2-x} electrodes, respectively, as presented in Figure 5e and Figure S3. The circuit in Figure 5e can be used to simulate the resistance in HER, which may be related to the interface properties of the electrolyte. Charge transfer resistance (R_{ct}) value of prepared catalysts can be subsequently derived according to the diameter of the Nyquist plots in Figure 5e and Figure S4, where R_{ct} of Se−CoS_{2-x} electrode (78.9 Ω) is much smaller than that of CoO_x (∼1190 Ω) and CoS_{2-x} (∼300 Ω), reflecting faster electrocatalytic kinetics and reaction rate. The stability test result (Figure 5f) indicates that the as-prepared electrode material has excellent stability, which can almost maintain its current density even after 2000 cycles durability test.

The C_{dl} value is calculated to evaluate the electrochemical active surface area (ECSA) of the catalysts,[46] as shown in parts a and b of Figure 6 and Figure S4. The C_{dl} value of the Se−CoS_{2-x} electrode is calculated to be 2.66 mF cm^{-2}, far more than that for CoS_2 (∼0.49 mF cm^{-2}), suggesting that Se−CoS_{2-x} has more exposed active sites and defects than CoS_{2-x}, which can explain the enhancement of the HER activity after Se doping. Herein, all of the as-prepared samples possess a similar nanorod morphology, and the greatly improved C_{dl} results of Se−CoS_{2-x} may be ascribed to an increase in the active sites arising from its polyporous-rod-like structure and Se doping factors. Parts c and d of Figure 6 illustrate CP curves of the Se−CoS_{2-x} electrode under varying overpotential. With increasing overpotential, the current density of the Se−CoS_{2-x} electrode rises accordingly and stabilizes soon, indicating outstanding mass transfer performance and mechanical stability of the Se−CoS_{2-x} electrode under acidic conditions.

The LSV curve in Figure 7a demonstrates the excellent HER and OER characteristics of Se−CoS_{2-x} catalysts under alkaline conditions. As shown in Figure 7b, the current density remains unchanged at a bias voltage of −0.5 V, manifesting strong long-term durability of the Se−CoS_{2-x} catalyst for HER. parts c and d of Figure 7 illustrate CP curves of the Se−CoS_{2-x} under varying overpotentials. Upon increasing the overpotential, the current densities of the Se−CoS_{2-x} electrode rise and soon stabilize. The results indicate that Se−CoS_{2-x} electrode has outstanding mass transfer performance and mechanical stability under alkaline condition.

The relative effective surface area is assessed to evaluate the catalytic performance by comparing the above values of C_{dl}. Table 1 shows that the addition of Se element into CoS_{2-x} material can effectively increase chemical specific surface area,

https://doi.org/10.1021/acsomega.1c03019
ACS Omega 2021, 6, 23300−23310

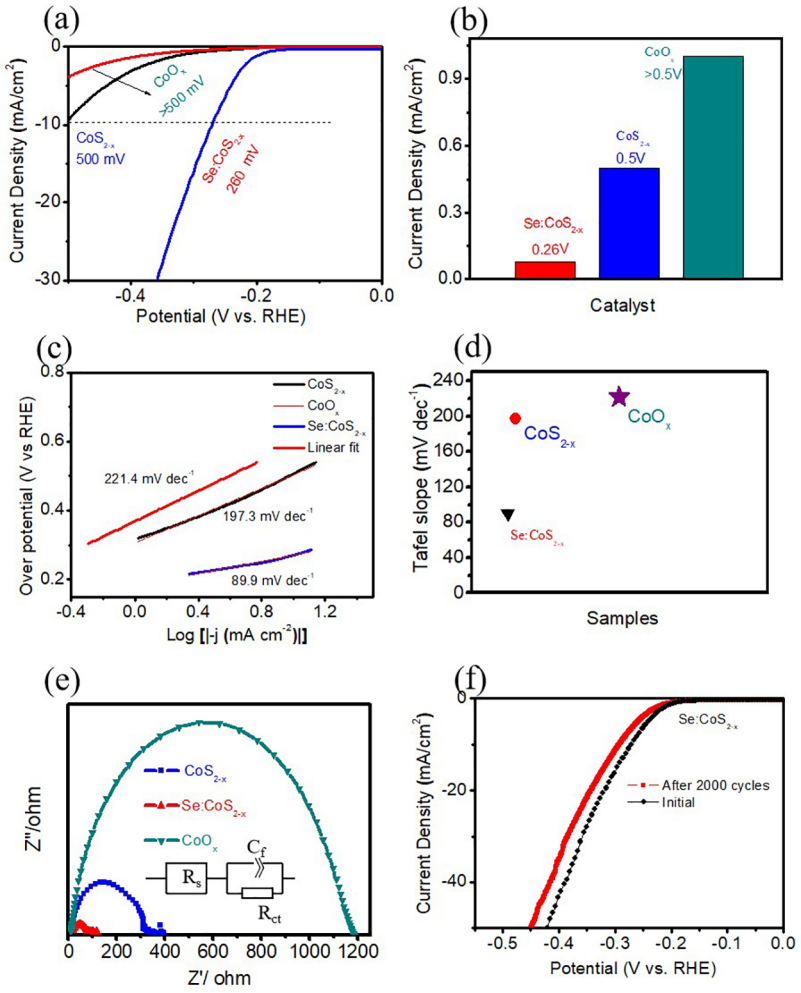

Figure 5. (a) LSV curves of CoO_x, CoS_{2-x} and Se−CoS_{2-x} at a scan rate of 5 mV s^{-1} in 0.5 M H_2SO_4. (b) Summary of the overpotential at j = 10 mA cm^{-2} of prepared catalysts. (c) Corresponding Tafel slope of all catalysts. (d) Tafel slope diagram of different catalysts. (e) EIS Nyquist plots of CoO_x, CoS_{2-x} and Se−CoS_{2-x} at 0.8 V. (f) Initial polarization curve of the Se−CoS_{2-x} electrode and after 2000 cycles.

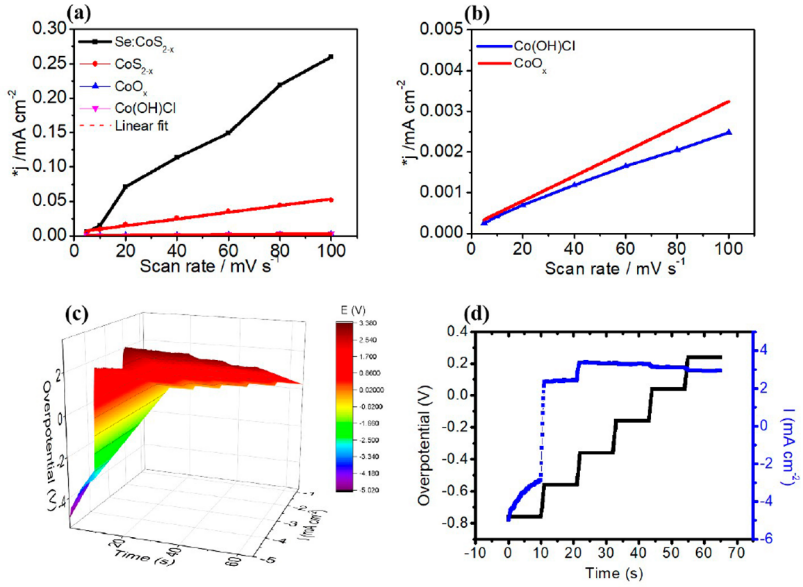

Figure 6. (a, b) C_{dl} of catalysts at 0.13 V versus RHE. (c, d) The multistep chronopotentiometric (CP) curve of Se−CoS_{2-x} catalysts under acidic conditions.

https://doi.org/10.1021/acsomega.1c03019
ACS Omega 2021, 6, 23300−23310

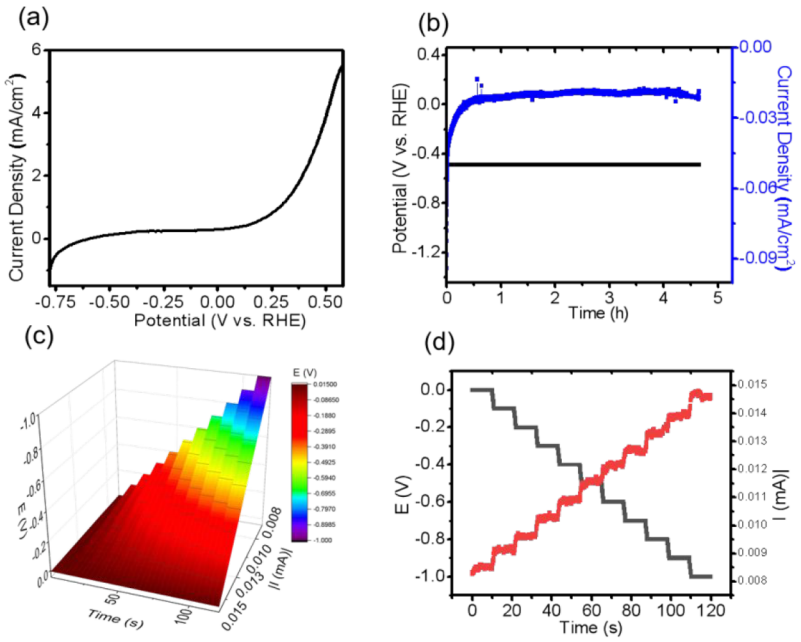

Figure 7. (a) LSV curve of Se−CoS_{2-x} with scan rate of 1 mV s^{-1} in 1 M KOH. (b) Time-dependent current density of Se−CoS_{2-x} catalysts. (c, d) Multistep chronopotentiometric curves of Se−CoS_{2-x} catalysts under alkaline conditions.

Table 1. Comparison Table of HER Performances of CoS_{2-x} and Se−CoS_{2-x} Samples

electrodes	η/mV	Tafel slope/mV dec^{-1}	C_{dl} [a]/mF cm^{-2}	R_{ct} [b]/Ω
Pt/C	29	29.03	–	29.3
Se−CoS_{2-x}	260	89.9	2.66	78.9
CoS_{2-x}	500	197.3	0.4	316.2
CoO_x	>500	221.4	0.03	1190

[a]Double-layer (C_{dl}). [b]Charge transfer (R_{ct}).

leading to better catalytic performance. From the chart below, conclusions can be drawn that (i) sulfur and selenium play significant roles in the HER process. Higher electrocatalytic activity of Se−CoS_{2-x} electrode indicates that the contribution of combined Co−Se−S is higher than sole sulfur during the reaction process. (ii) When Se element is doped into the CoS_{2-x} crystal, Se^{2-} will replace the part position of S^{2-}, leading to wider crystal surface spacing between Co−S−Se bonds, which is conducive to the transfer of catalyst at the interface.

In order to better investigate the effects of Se doping in CoS_2, geometric and electronic structures of the system are calculated via density functional theory (DFT). Parts a and b of Figure 8 display the crystal structure models of pristine CoS_2 and Se−CoS_2. The introduction of Se leads to the substitution of some S atoms by Se. Parts c and d of Figure 8 show band structures and density of states (DOS) plots. The almost identical distribution of CoS_2 and Se−CoS_2 means that Se doping can keep the excellent electronic properties of CoS_2. Then, two possible sites on CoS_2 and Se−CoS_2 have been examined, that is, the Co-site and the S-site. The Bader charge is analyzed to investigate the electron transfer, as shown in Figure 8e. It can be seen that for all the structure, the charge transfer have a similar behavior before and after Se doping for both the Co-site and the S-site, respectively. This means that the mechanism of adsorption has not changed. Free energy difference of H (ΔG_{H^*}) is then calculated (Figure 8f) to assess the activity of the surfaces. It can be inferred that Co atoms in CoS_2 and Se:CoS_2 are the active sites for HER, since the ΔG_{H^*} of the Co-site is much closer to zero than that of the S-site. The calculated values of the Co-site and the S-site both show reduction after Se doping (0.44 and 0.86 eV for CoS_2, 0.39 and 0.84 eV for Se-doped CoS_2. Observing the lower ΔG_{H^*} of the Co-site after doping with Se, it can be deduced that the Se dopant can reduce the HER energy barrier and promote the hydrogen evolution. Considering that the free energy is related to the doping concentration and structure, another Se-doped CoS_2 system has been calculated (Figure S8). And it shows a similar Bader charge value and lower free energy value (0.33 eV for the Co-site and 0.75 eV for the S-site), confirming that the Se dopant can reduce the HER energy barrier and the structure can effect the free energy. This signifies the importance of Se in Se−CoS_2 and validates its superior electrocatalytic HER activity over CoS_2 as obtained experimentally.

CONCLUSIONS

In summary, the porous Se−CoS_{2-x} nanorod is successfully synthesized by a facile two-step method. The as-prepared Se−CoS_{2-x} electrode exhibits much improved catalytic activity, which may be attributed to the reasons as follows: (i) Under a high temperature reaction, the formation of defects in the catalyst caused by Se doping may provide more active sites, thus improving the performance of hydrogen evolution. (ii) The larger electronegativity of Se atom than S atom makes Co−Se bond easier to form. (iii) The synergic effects of Se doping and CoS_2 catalyst support are obseved. (iv) When Se elements are doped into the CoS_2 crystal, Se^{2-} will partly replace the position of S^{2-} and the crystal surface spacing between Co−S−Se bonds will be wider, which is conducive to the transfer of catalyst at the interface. In this paper, the Se−CoS_{2-x} catalyst shows excellent HER performance, such as low overpotential (~260 mV for current density of 10 mA cm^{-2}), low Tafel slope (89.9 mV dec^{-1}), and outstanding mass transfer property and mechanical robustness. The above results

https://doi.org/10.1021/acsomega.1c03019
ACS Omega 2021, 6, 23300−23310

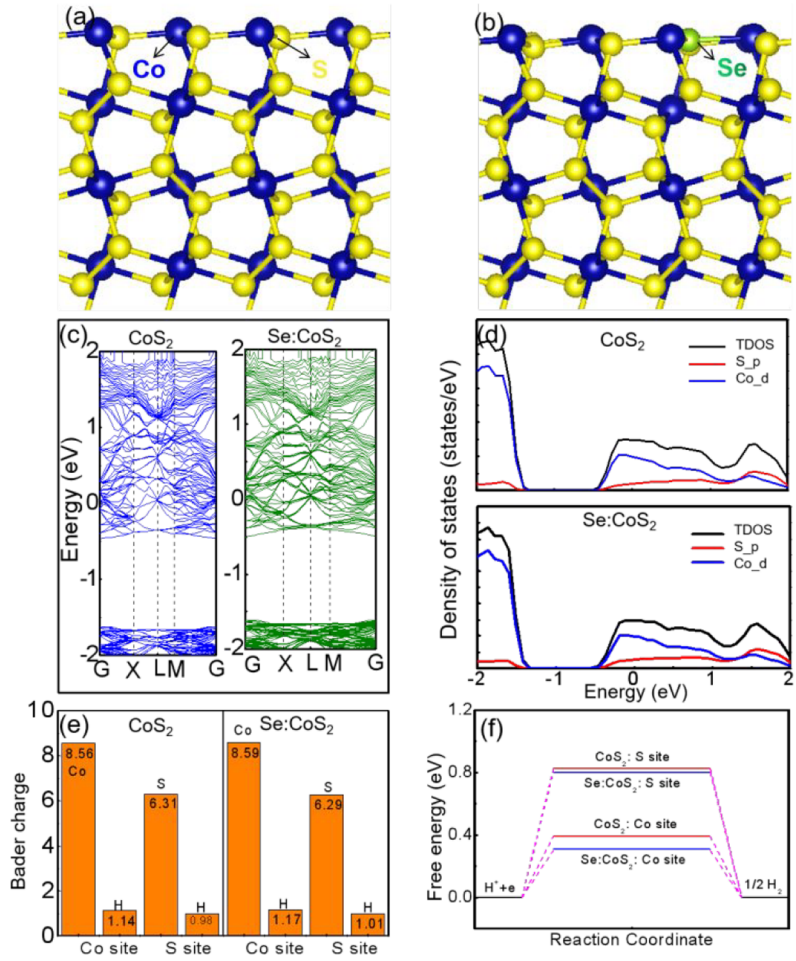

Figure 8. (a, b) Crystal structures of CoS_2 and Se−CoS_2, respectively. (c) Electronic band structures of CoS_2 and Se−CoS_2. (d) PDOS plots of CoS_2 and Se−CoS_2. (e) Calculated Bader charges of Co, S, and H atoms for CoS_2 and Se−CoS_2, respectively. (f) Gibbs free energy of CoS_2 and Se−CoS_2 (Co-sites and S-sites).

indicate that doping can greatly enhance the electrochemical catalytic property, and this strategy may be applied to other TMDs materials for energy storage-related applications.

EXPERIMENTAL SECTION

Synthesis of Co(OH)Cl UNs. Typically, 2 mmol of $CoCl_2$ or $CoCl_2{\cdot}6H_2O$, 7 mmol of NH_4Cl, and 9 mmol of urea were dissolved in deionized water (35 mL). After being fully stirred, the obtained solution was transferred into a reaction vessel (a 50 mL autoclave) and then placed in an oven at 140 °C. After 6−12 h of constant temperature reaction, the autoclave was taken out from the oven for cooling to room temperature. The obtained product was then washed with absolute ethanol for several times, and finally dried overnight under vacuum at 60 °C.

Synthesis of CoO_x. The annealing process is as follows: 0.01 g of Co(OH)Cl UNs samples were located at the high-temperature zone of a tube furnace, the heating zone was heated to 400 °C with heating rate of 6 °C/min, the whole process was carried out in Ar atmosphere, and the final product was obtained after 1 h of reaction.

Synthesis of Porous Rod-like Cobalt Sulfides. The sulfurization process is described as in our previous work:[57] First 0.01 g of Co(OH)Cl UNs sample was located at the high-temperature zone of a tube furnace, and S powder (0.1 g) was located at the upstream side of the tube furnace, being about 15 cm apart. The upstream zone was heated to 250 °C with a heating rate of 6 °C/min, and the downstream zone was heated to 400 °C with a heating rate of 10 °C/min. The whole process was carried out in an Ar atmosphere, and the final product was obtained after 1 h reaction.

Synthesis of Porous Rod-like Se-Doped Cobalt Sulfides. The whole process was almost identical as described in the previous procedure of synthesizing cobalt sulfides, except for replacing the S powder (0.1 g) with a mixture of S powder (0.08 g) and Se powder (0.02 g).

Characterization. Field emission scanning electron microscopy (FESEM, SU8010, Hitachi Japan and TESCAN MIRA3) and field emission transmission electron microscopy (FETEM, JEM2100F, 200 kV) were used to characterize the microstructure and morphologies of samples. The chemical components and elemental state of the samples were detected via X-ray photoelectron spectroscopy (XPS, Escalab 250Xi, Al Kα, USA). The crystallite structures of the products were observed by using X-ray diffraction (XRD, Xpert Pro MPD diffractometer, Cu Kα radiation).

Preparation of Electrode. The electrode was prepared using the method we have reported before.[62] The dispersion solution composed of 4 mg of sample, 30 μL of Nafion solution (5 wt %), and 1:4 mixed solution of water (200 μL)

https://doi.org/10.1021/acsomega.1c03019
ACS Omega 2021, 6, 23300−23310

and ethanol (800 μL), was placed under ultrasonic vibration for about 1 h to form a homogeneous catalyst ink. Then 5 μL of the dispersion solution was loaded onto a working electrode (glassy carbon electrode, diameter d = 3 mm). The catalyst was about 0.285 mg cm^{-2}.

Electrochemical Measurement. A three-electrode test system was adopted (working electrode, glassy carbon electrode; reference electrode, Ag/AgCl (saturated KCl) electrode; and counter electrode, graphite rod). Electrochemical hydrogen evolution performance test of all samples were completed by CHI660E electrochemical station and ZAHNER pro electrochemical workstation. The Linear sweep voltammetry (LSV) was performed in 0.5 M H_2SO_4 solution (pure N_2). The potential of reversible hydrogen electrode (RHE) was calibrated as $E_{RHE} = E_{Ag/AgCl} + 0.217$ V.[28] The HER stability of all catalysts were tested by an amperometric i−t curve with a scan rate of 100 mV s^{-1}. The double-layer capacitances (C_{dl}) were estimated by CV in the range of 0.08−0.19 V versus RHE region at various scan rates (5−100 mV s^{-1}). The electrochemical impedance spectroscopy (EIS) was tested with an AC voltage of 0.8 V over the frequencies 0.1−10^5 Hz.

DFT Calculations. The geometric and electronic structures of systems were calculated via density functional theory (DFT), and implemented in the Vienna ab initio simulation package (VASP).[58] The interactions between valence electrons and ionic cores were described by the projector-augmented wave (PAW) method, and the electron exchange and correlation were described by generalized gradient approximation (GGA) functional of Perdew, Burke, and Ernzerhof (PBE).[59] In the calculation, the force convergence criterion and energy convergence criterion was set to be 0.01 eV/Å and 10^{-5} eV, respectively. The cutoff energy was set as 450 eV. The Monkhorst−Pack grid was set to be 7 × 7 × 7 and 7 × 7 × 1 to the first Brillouin zone for bulk and surface systems, respectively.

■ ASSOCIATED CONTENT

Supporting Information

The Supporting Information is available free of charge at https://pubs.acs.org/doi/10.1021/acsomega.1c03019.

SEM images of precursor Co(OH)Cl UNs and the wide spectrum of Se−CoS_{2-x} nanorod (PDF)

■ AUTHOR INFORMATION

Corresponding Author

Zhihong Zhu − *College of Advanced Interdisciplinary Studies & Hunan Provincial Key Laboratory of Novel Nano-Optoelectronic Information Materials and Devices, National University of Defense Technology, Changsha 410073, China;* orcid.org/0000-0003-3199-9323; Email: zzhwcx@163.com

Authors

Zhengtian Shi − *College of Advanced Interdisciplinary Studies & Hunan Provincial Key Laboratory of Novel Nano-Optoelectronic Information Materials and Devices, National University of Defense Technology, Changsha 410073, China*

Xiangqian Qi − *College of Advanced Interdisciplinary Studies & Hunan Provincial Key Laboratory of Novel Nano-Optoelectronic Information Materials and Devices, National University of Defense Technology, Changsha 410073, China*

Zhiyuan Zhang − *College of Advanced Interdisciplinary Studies & Hunan Provincial Key Laboratory of Novel Nano-Optoelectronic Information Materials and Devices, National University of Defense Technology, Changsha 410073, China*

Yingchao Song − *College of Advanced Interdisciplinary Studies & Hunan Provincial Key Laboratory of Novel Nano-Optoelectronic Information Materials and Devices, National University of Defense Technology, Changsha 410073, China*

Jianfa Zhang − *College of Advanced Interdisciplinary Studies & Hunan Provincial Key Laboratory of Novel Nano-Optoelectronic Information Materials and Devices, National University of Defense Technology, Changsha 410073, China;* orcid.org/0000-0001-5879-5633

Chucai Guo − *College of Advanced Interdisciplinary Studies & Hunan Provincial Key Laboratory of Novel Nano-Optoelectronic Information Materials and Devices, National University of Defense Technology, Changsha 410073, China*

Complete contact information is available at: https://pubs.acs.org/10.1021/acsomega.1c03019

Author Contributions

†Z.S., X.Q., and Z.Zhang contributed equally to this study.

Notes

The authors declare no competing financial interest.

■ ACKNOWLEDGMENTS

This work is financially supported by the Natural National Science Foundation of China (NSFC) (11674396).

■ REFERENCES

(1) McCollum, D. L.; Jewell, J.; Krey, V.; Bazilian, M.; Fay, M.; Riahi, K. Quantifying uncertainties influencing the long-term impacts of oil prices on energy markets and carbon emissions. *Nat. Energy* **2016**, *1*, 77−84.

(2) McFarland, E. Unconventional Chemistry for Unconventional Natural Gas. *Science* **2012**, *338*, 340−343.

(3) Jewell, J.; McCollum, D.; Emmerling, J.; Bertram, C.; Gernaat, D. E. H. J.; Krey, V.; Paroussos, L.; Berger, L.; Fragkiadakis, K.; Keppo, I.; Saadi, N.; Tavoni, M.; van Vuuren, D.; Vinichenko, V.; Riahi, K. Limited emission reductions from fuel subsidy removal except in energy-exporting regions. *Nature* **2018**, *554*, 229−233.

(4) Qiu, Y.; Liu, W.; Chen, W.; Chen, W.; Zhou, G.; Hsu, P.-C.; Zhang, R.; Liang, Z.; Fan, S.; Zhang, Y.; Cui, Y. Efficient solar-driven water splitting by nanocone $BiVO_4$-perovskite tandem cells. *Sci. Adv.* **2016**, *2*, e1501764.

(5) Chong, L.; Wen, J.; Kubal, J.; Sen, F. G.; Zou, J.; Greeley, J.; Chan, M.; Barkholtz, H.; Ding, W.; Liu, D.-J. Ultralow-loading platinum-cobalt fuel cell catalysts derived from imidazolate frameworks. *Science* **2018**, *362*, 1276−1281.

(6) Mao, J.; Chen, W.; He, D.; Wan, J.; Pei, J.; Dong, J.; Wang, Y.; An, P.; Jin, Z.; Xing, W.; Tang, H.; Zhuang, Z.; Liang, X.; Huang, Y.; Zhou, G.; Wang, L.; Wang, D.; Li, Y. Design of ultrathin Pt-Mo-Ni nanowire catalysts for ethanol electrooxidation. *Sci. Adv.* **2017**, *3*, e1603068.

(7) Wang, L.; Chen, M.-X.; Yan, Q.-Q.; Xu, S.-L.; Chu, S.-Q.; Chen, P.; Lin, Y.; Liang, H.-W. A sulfur-tethering synthesis strategy toward high-loading atomically dispersed noble metal catalysts. *Sci. Adv.* **2019**, *5*, eaax6322.

(8) Shi, Z.-T.; Kang, W.; Xu, J.; Sun, Y.-W.; Jiang, M.; Ng, T.-W.; Xue, H.-T.; Yu, D. Y. W.; Zhang, W.; Lee, C.-S. Hierarchical nanotubes assembled from MoS_2-carbon monolayer sandwiched superstructure nanosheets for high-performance sodium ion batteries. *Nano Energy* **2016**, *22*, 27−37.

(9) Zhang, X.; Grajal, J.; Vazquez-Roy, J. L.; Radhakrishna, U.; Wang, X.; Chern, W.; Zhou, L.; Lin, Y.; Shen, P.-C.; Ji, X.; Ling, X.;

Zubair, A.; Zhang, Y.; Wang, H.; Dubey, M.; Kong, J.; Dresselhaus, M.; Palacios, T. Two-dimensional MoS_2-enabled flexible rectenna for Wi-Fi-band wireless energy harvesting. *Nature* **2019**, *566*, 368−372.
(10) Li, H.; Wang, J.; Gao, S.; Chen, Q.; Peng, L.; Liu, K.; Wei, X. Superlubricity between MoS_2 Monolayers. *Adv. Mater.* **2017**, *29*, 1701474.
(11) Shi, Z.-T.; Kang, W.; Xu, J.; Sun, L.-L.; Wu, C.; Wang, L.; Yu, Y.-Q.; Yu, D. Y. W.; Zhang, W.; Lee, C.-S. In Situ Carbon-Doped $Mo(Se_{0.85}S_{0.15})_2$ Hierarchical Nanotubes as Stable Anodes for High-Performance Sodium-Ion Batteries. *Small* **2015**, *11*, 5667−5674.
(12) Kim, S.; Maassen, J.; Lee, J.; Kim, S. M.; Han, G.; Kwon, J.; Hong, S.; Park, J.; Liu, N.; Park, Y. C.; Omkaram, I.; Rhyee, J.-S.; Hong, Y. K.; Yoon, Y. Interstitial Mo-Assisted Photovoltaic Effect in Multilayer $MoSe_2$ Phototransistors. *Adv. Mater.* **2018**, *30*, 1705542−1705550.
(13) Bellani, S.; Wang, F.; Longoni, G.; Najafi, L.; Oropesa-Nuñez, R.; Del Rio Castillo, A. E.; Prato, M.; Zhuang, X.; Pellegrini, V.; Feng, X.; Bonaccorso, F. WS_2-Graphite Dual-Ion Batteries. *Nano Lett.* **2018**, *18*, 7155−7164.
(14) Asadi, M.; Kim, K.; Liu, C.; Addepalli, A. V.; Abbasi, P.; Yasaei, P.; Phillips, P.; Behranginia, A.; Cerrato, J. M.; Haasch, R.; Zapol, P.; Kumar, B.; Klie, R. F.; Abiade, J.; Curtiss, L. A.; Salehi-Khojin, A. Nanostructured transition metal dichalcogenide electrocatalysts for CO_2 reduction in ionic liquid. *Science* **2016**, *353*, 467.
(15) Yu, L.; Yang, J. F.; Lou, X. W. D. Formation of CoS_2 Nanobubble Hollow Prisms for Highly Reversible Lithium Storage. *Angew. Chem., Int. Ed.* **2016**, *55*, 13422−13426.
(16) Faber, M. S.; Dziedzic, R.; Lukowski, M. A.; Kaiser, N. S.; Ding, Q.; Jin, S. High-Performance Electrocatalysis Using Metallic Cobalt Pyrite (CoS_2) Micro-and Nanostructures. *J. Am. Chem. Soc.* **2014**, *136*, 10053−10061.
(17) Ai, G.; Hu, Q.; Zhang, L.; Dai, K.; Wang, J.; Xu, Z.; Huang, Y.; Zhang, B.; Li, D.; Zhang, T.; Liu, G.; Mao, W. Investigation of the Nanocrystal CoS_2 Embedded in 3D Honeycomb-like Graphitic Carbon with a Synergistic Effect for High-Performance Lithium Sulfur Batteries. *ACS Appl. Mater. Interfaces* **2019**, *11*, 33987−33999.
(18) Jin, J.; Zhang, X.; He, T. Self-Assembled CoS_2Nanocrystal Film as an Efficient Counter Electrode for Dye-Sensitized Solar Cells. *J. Phys. Chem. C* **2014**, *118*, 24877−24883.
(19) Pan, Y.; Cheng, X.; Gong, L.; Shi, L.; Zhou, T.; Deng, Y.; Zhang, H. Double-Morphology CoS_2 Anchored on N-Doped Multichannel Carbon Nanofibers as High-Performance Anode Materials for Na-Ion Batteries. *ACS Appl. Mater. Interfaces* **2018**, *10*, 31441−31451.
(20) Huang, L.; Han, B.; Xi, Y.; Forrey, R. C.; Cheng, H. Influence of Charge on the Reactivity of Supported Heterogeneous Transition Metal Catalysts. *ACS Catal.* **2015**, *5*, 4592−4597.
(21) Price, S. W. T.; Martin, D. J.; Parsons, A. D.; Sławinski, W. A.; Vamvakeros, A.; Keylock, S. J.; Beale, A. M.; Mosselmans, J. F. W. Chemical imaging of Fischer−Tropsch catalysts under operating conditions. *Sci. Adv.* **2017**, *3*, e1602838.
(22) Nazimov, D. A.; Klimov, O. V.; Shaverina, A. V.; Cherepanova, S. V.; Larina, T. V.; Khabibulin, D. F.; Noskov, A. S. The Effect of Transition Alumina (γ-, η-, χ-Al_2O_3) on the Activity and Stability of Chromia/Alumina Catalysts. *Energy Technol.* **2019**, *7*, 1800736−1800743.
(23) Zhang, L.; Wang, T.; Sun, L.; Sun, Y.; Hu, T.; Xu, K.; Ma, F. Hydrothermal synthesis of 3D hierarchical $MoSe_2$/$NiSe_2$ composite nanowires on carbon fiber paper and their enhanced electrocatalytic activity for the hydrogen evolution reaction. *J. Mater. Chem. A* **2017**, *5*, 19752−19759.
(24) Zhang, K.; Park, M.; Zhou, L.; Lee, G.-H.; Li, W.; Kang, Y.-M.; Chen, J. Urchin-Like $CoSe_2$ as a High-Performance Anode Material for Sodium-Ion Batteries. *Adv. Funct. Mater.* **2016**, *26*, 6728−6735.
(25) Gao, M.-R.; Cao, X.; Gao, Q.; Xu, Y.-F.; Zheng, Y.-R.; Jiang, J.; Yu, S.-H. Nitrogen-Doped Graphene Supported $CoSe_2$ Nanobelt Composite Catalyst for Efficient Water Oxidation. *ACS Nano* **2014**, *8*, 3970−3978.
(26) Gui, Y.; Liu, X.; Dou, Y.; Zhang, L.; Al-Mamun, M.; Jiang, L.; Yin, H.; He, C.-T.; Zhao, H. Manipulating the assembled structure of atomically thin $CoSe_2$ nanomaterials for enhanced water oxidation catalysis. *Nano Energy* **2019**, *57*, 371−378.
(27) Yin, H.; Qu, H.-Q.; Liu, Z.; Jiang, R.-Z.; Li, C.; Zhu, M.-Q. Long cycle life and high rate capability of three dimensional $CoSe_2$ grain-attached carbon nanofibers for flexible sodium-ion batteries. *Nano Energy* **2019**, *58*, 715−723.
(28) Xia, Z.; Sun, H.; He, X.; Sun, Z.; Lu, C.; Li, J.; Peng, Y.; Dou, S.; Sun, J.; Liu, Z. In situ construction of $CoSe_2$@vertical-oriented graphene arrays as self-supporting electrodes for sodium-ion capacitors and electrocatalytic oxygen evolution. *Nano Energy* **2019**, *60*, 385−393.
(29) Fang, Y.; Yu, X. Y.; Lou, X. W. D. Formation of Hierarchical Cu-Doped $CoSe_2$Microboxes via Sequential Ion Exchange for High-Performance Sodium-Ion Batteries. *Adv. Mater.* **2018**, *30*, 1706668−106673.
(30) Tabassum, H.; Zhi, C.; Hussain, T.; Qiu, T.; Aftab, W.; Zou, R. Encapsulating Trogtalite $CoSe_2$ Nanobuds into BCN Nanotubes as High Storage Capacity Sodium Ion Battery Anodes. *Adv. Energy Mater.* **2019**, *9*, 1901778−1901787.
(31) Li, M.; Qian, Y.; Du, J.; Wu, H.; Zhang, L.; Li, G.; Li, K.; Wang, W.; Kang, D. J. CuS Nanosheets Decorated with CoS_2Nanoparticles as an Efficient Electrocatalyst for Enhanced Hydrogen Evolution at All pH Values. *ACS Sustainable Chem. Eng.* **2019**, *7*, 14016−14022.
(32) Hou, J.; Zhang, B.; Li, Z.; Cao, S.; Sun, Y.; Wu, Y.; Gao, Z.; Sun, L. Vertically Aligned Oxygenated-CoS_2-MoS_2 Heteronanosheet Architecture from Polyoxometalate for Efficient and Stable Overall Water Splitting. *ACS Catal.* **2018**, *8*, 4612−4621.
(33) Han, X.; Wu, X.; Deng, Y.; Liu, J.; Lu, J.; Zhong, C.; Hu, W. Ultrafine Pt Nanoparticle-Decorated Pyrite-Type CoS_2 Nanosheet Arrays Coated on Carbon Cloth as a Bifunctional Electrode for Overall Water Splitting. *Adv. Energy Mater.* **2018**, *8*, 1800935−1800946.
(34) Li, Q.; Xing, Z.; Wang, D.; Sun, X.; Yang, X. In Situ Electrochemically Activated CoMn-S@NiO/CC Nanosheets Array for Enhanced Hydrogen Evolution. *ACS Catal.* **2016**, *6*, 2797−2801.
(35) Gao, J.; Liang, G.; Zhang, B.; Kuang, Y.; Zhang, X.; Xu, B. FePt@CoS_2 Yolk-Shell Nanocrystals as a Potent Agent to Kill HeLa Cells. *J. Am. Chem. Soc.* **2007**, *129*, 1428−1433.
(36) Fang, Y.; Guan, B. Y.; Luan, D.; Lou, X. W. Synthesis of CuS@CoS_2 Double-Shelled Nanoboxes with Enhanced Sodium Storage Properties. *Angew. Chem., Int. Ed.* **2019**, *58*, 7739−7743.
(37) Fang, Y.; Guan, B.; Luan, D.; Lou, X. W. D. Elegant Synthesis of CuS@CoS_2 Double-Shelled Nanoboxes with Enhanced Sodium Storage Properties. *Angew. Chem.* **2019**, *131*, 7821−7825.
(38) Yan, S.; Wang, K.; Zhou, F.; Lin, S.; Song, H.; Shi, Y.; Yao, J. Ultrafine Co:FeS_2/CoS_2 Heterostructure Nanowires for Highly Efficient Hydrogen Evolution Reaction. *ACS Appl. Mater. Interfaces* **2020**, *3*, 514−520.
(39) Zhang, J.; Xiao, W.; Xi, P.; Xi, S.; Du, Y.; Gao, D.; Ding, J. Activating and Optimizing Activity of CoS_2 for Hydrogen Evolution Reaction through the Synergic Effect of N Dopants and S Vacancies. *ACS Energy Lett.* **2017**, *2*, 1022−1028.
(40) He, G.; Zhang, W.; Deng, Y.; Zhong, C.; Hu, W.; Han, X. Engineering Pyrite-Type Bimetallic Ni-Doped CoS_2 Nanoneedle Arrays over a Wide Compositional Range for Enhanced Oxygen and Hydrogen Electrocatalysis with Flexible Property. *Catalysts* **2017**, *7*, 366−382.
(41) Chen, P.; Zhou, T.; Chen, M.; Tong, Y.; Zhang, N.; Peng, X.; Chu, W.; Wu, X.; Wu, C.; Xie, Y. Enhanced Catalytic Activity in Nitrogen-Anion Modified Metallic Cobalt Disulfide Porous Nanowire Arrays for Hydrogen Evolution. *ACS Catal.* **2017**, *7*, 7405−7411.
(42) Guo, L.; Deng, J.; Wang, G.; Hao, Y.; Bi, K.; Wang, X.; Yang, Y. N, P-doped CoS_2Embedded in TiO_2 Nanoporous Films for Zn-Air Batteries. *Adv. Funct. Mater.* **2018**, *28*, 1804540−1804547.
(43) Pan, Y.; Cheng, X.; Gong, L.; Shi, L.; Zhang, H. Nanoflower-like N-doped C/CoS_2 as high-performance anode materials for Na-ion batteries. *Nanoscale* **2018**, *10*, 20813−20820.

https://doi.org/10.1021/acsomega.1c03019
ACS Omega 2021, 6, 23300−23310

(44) Hao, J.; Yang, W.; Peng, Z.; Zhang, C.; Huang, Z.; Shi, W. A Nitrogen Doping Method for CoS_2 Electrocatalysts with Enhanced Water Oxidation Performance. *ACS Catal.* **2017**, *7*, 4214−4220.
(45) Zhang, J.; Xiao, W.; Xi, P.; Xi, S.; Du, Y.; Gao, D.; Ding, J. Activating and Optimizing Activity of CoS_2 for Hydrogen Evolution Reaction through the Synergic Effect of N Dopants and S Vacancies. *ACS Energy Lett.* **2017**, *2*, 1022−1028.
(46) Chen, C.-J.; Liu, C.-W.; Yang, K.-C.; Yin, L.-C.; Wei, D.-H.; Hu, S.-F.; Liu, R.-S. Amorphous Phosphorus-Doped Cobalt Sulfide Modified on Silicon Pyramids for Efficient Solar Water Reduction. *ACS Appl. Mater. Interfaces* **2018**, *10*, 37142−37149.
(47) Zhang, J.; Liu, Y.; Xia, B.; Sun, C.; Liu, Y.; Liu, P.; Gao, D. Facile one-step synthesis of phosphorus-doped CoS_2 as efficient electrocatalyst for hydrogen evolution reaction. *Electrochim. Acta* **2018**, *259*, 955−961.
(48) Zhang, Y.-Y.; Zhang, X.; Wu, Z.-Y.; Zhang, B.-B.; Zhang, Y.; Jiang, W.-J.; Yang, Y.-G.; Kong, Q.-H.; Hu, J.-S. Fe/P Dual Doping Boosts the Activity and Durability of CoS_2 Polycrystalline Nanowires for Hydrogen Evolution. *J. Mater. Chem. A* **2019**, *7*, 5195−5200.
(49) Ouyang, C.; Wang, X.; Wang, S. Phosphorus-Doped CoS_2 Nanosheet Arrays as Ultra-efficient Electrocatalysts for Hydrogen Evolution Reaction. *Chem. Commun.* **2015**, *51*, 14160−14163.
(50) Zhang, J.; Liu, Y.; Xia, B.; Sun, C.; Liu, Y.; Liu, P.; Gao, D. Facile one-step synthesis of phosphorus-doped CoS_2 as efficient electrocatalyst for hydrogen evolution reaction, Electrochim. *Electrochim. Acta* **2018**, *259*, 955−961.
(51) Xie, Z.; Tang, H.; Wang, Y. MOF-Derived Ni-Doped CoS_2 Grown on Carbon Fiber Paper for Efficient Oxygen Evolution Reaction. *ChemElectroChem* **2019**, *6*, 1206−1212.
(52) Kong, W.; Luan, X.; Du, H.; Xia, L.; Qu, F. Enhanced electrocatalytic activity of water oxidation in alkaline medium by Fe doping in CoS_2 nanosheet. *Chem. Commun.* **2019**, *55*, 2469−2472.
(53) Lu, J.; Cai, L.; Zhang, N.; Qiu, B.; Chai, Y. Robust Photoelectrochemical Oxygen Evolution with N, Fe-CoS_2 Nanorod Arrays. *ACS Appl. Mater. Interfaces* **2019**, *11*, 44214−44222.
(54) Wang, M.; Zhang, W.; Zhang, F.; Zhang, Z.; Tang, B.; Li, J.; Wang, X. Theoretical Expectation and Experimental Implementation of In Situ Al-Doped CoS_2 Nanowires on Dealloying-Derived Nanoporous Intermetallic Substrate as an Efficient Electrocatalyst for Boosting Hydrogen Production. *ACS Catal.* **2019**, *9*, 1489−1502.
(55) Wang, Y.; Jian, C.; Hong, W.; Cai, Q.; Liu, W. Tuning the electron status of urchin-like CoS_2nanowires by selenium doping toward highly efficient hydrogen evolution reaction. *Mater. Lett.* **2019**, *257*, 126673−126676.
(56) Zhang, J.; Liu, Y.; Sun, C.; Xi, P.; Peng, S.; Gao, D.; Xue, D. Accelerated Hydrogen Evolution Reaction in CoS_2 by Transition-Metal Doping. *ACS Energy Lett.* **2018**, *3*, 779−786.
(57) Shi, Z. T.; Qi, Y.; Zhang, J.; Guo, C. C.; Zhu, Z. H. Carbon-Based Metallic Cobalt Pyrite Nanotubes as Stable Electrode Materials for Electrochemical Hydrogen Evolution. *ACS Appl. Nano Mater.* **2020**, *3*, 8335−8342.
(58) Kresse, G.; Hafner, J. Ab initio molecular dynamics for liquid metals. *Phys. Rev. B: Condens. Matter Mater. Phys.* **1993**, *47*, 558−561.
(59) Perdew, J. P.; Burke, K.; Ernzerhof, M. Generalized gradient approximation made simple. *Phys. Rev. Lett.* **1996**, *77*, 3865−3868.

https://doi.org/10.1021/acsomega.1c03019
ACS Omega 2021, 6, 23300−23310